ACS APPLIED MATERIALS & INTERFACES

www.acsami.org

Research Article

Entropy-Stabilized Multication Fluorides as a Conversion-Type Cathode for Li-Ion Batteries—Impact of Element Selection

Jehee Park,* Yingjie Yang, Haesun Park, Aditya Sundar, Sungsik Lee, Tiffany L. Kinnibrugh, Seoung-bum Son, Eungje Lee, Peter Zapol, Robert F. Klie, and Jae Jin Kim*

Cite This: *ACS Appl. Mater. Interfaces* 2024, 16, 57151−57161

Read Online

ACCESS | Metrics & More | Article Recommendations | Supporting Information

ABSTRACT: Metal fluorides (e.g., FeF_2 and FeF_3) have received attention as conversion-type cathode materials for Li-ion batteries due to their higher theoretical capacity compared to that of common intercalation materials. However, their practical use has been hindered by low round-trip efficiency, voltage hysteresis, and capacity fading. Cation substitution has been proposed to address these challenges, and recent advancements in battery performance involve the introduction of entropy stabilization in an attempt to facilitate reversible conversion reactions by increasing configurational entropy. Building on this concept, high entropy fluorides with five cations were synthesized by using a simple mechanochemical route. In order to examine the impact of element selection, $Co_{0.2}Cu_{0.2}Ni_{0.2}Zn_{0.2}Fe_{0.2}F_2$ (HEF-Fe) was compared with $Co_{0.2}Cu_{0.2}Ni_{0.2}Zn_{0.2}Mg_{0.2}F_2$ (HEF-Mg), replacing electrochemically inactive Mg with Fe as an active participant in the conversion reaction. Combining electrochemical measurements with first-principles calculations, high-resolution electron microscopy, and synchrotron X-ray analysis, HEFs' battery performances and conversion reaction mechanisms were investigated in detail. The results highlighted that replacement of Mg with Fe was beneficial, with enhanced capacity, rate capability, and surface stability. In addition, it was found that HEF-Fe showed similar cycle stability without an electrochemically inactive element. These findings provide valuable insights for the design of high entropy multielement fluorides for improved Li-ion battery performance.

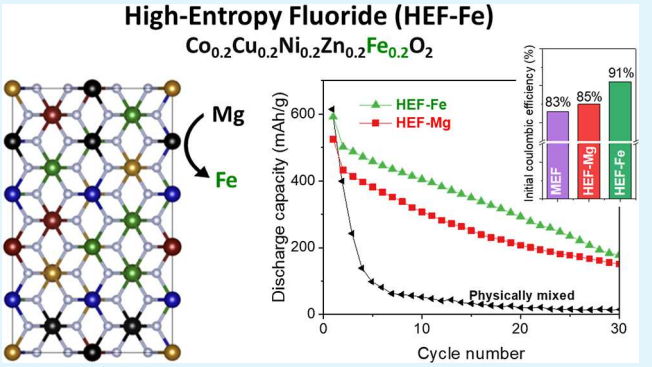

KEYWORDS: *high entropy materials, metal fluoride, conversion, cathode, Li-ion batteries*

1. INTRODUCTION

Metal fluorides have been studied as a conversion-type cathode material for Li-ion batteries due to higher theoretical capacity and potentially lower cost than typical intercalation materials.[1] For example, iron fluorides (FeF_2 and FeF_3) can provide higher theoretical capacity (571 and 712 mA h/g, respectively) than conventional cathode materials (e.g., $LiCoO_2$, Li-(NiMnCo)O_2, and $LiFePO_4$ deliver 140−170 mA h/g).[2] However, their practical use is limited due to the low round-trip efficiency, large voltage hysteresis, and capacity fading during cycling, which have primarily originated from substantial irreversible structural reorganization during conversion reaction.[3,4] To overcome these issues, cation substitution has been suggested to tune the electrochemical properties of metal fluorides. For example, substitution of Fe for Cu in CuF_2 was found to be effective to mitigate deleterious agglomeration/dissolution of Cu ions and allow reversible Cu^{2+}/Cu^0 redox reaction with the decreased voltage hysteresis.[5]

Recently, this approach has been expanded to the introduction of high entropy stabilization in order to achieve a reversible conversion reaction for Li storage. This concept involves stabilization of a single-phase structure by increasing configurational entropy to overcome enthalpy gain associated with phase separation.[6] With optimal elemental selection in consideration of interaction between incorporated elements, high entropy materials can offer an appealing opportunity of tailoring material's properties and performance, so-called "cocktail effect". A previous work by Breitung et al. proposed that more reversible conversion reaction could be achieved in a rock-salt-structured $Co_{0.2}Cu_{0.2}Ni_{0.2}Zn_{0.2}Mg_{0.2}O$ oxide by entropy stabilization.[7] In this high entropy oxide (HEO), elementally mixed phases are thermodynamically favored so that cation diffusion kinetics is expected to be sluggish leading to suppressed agglomeration and enhanced structural reversibility during conversion reaction as compared to lower configurational entropy materials.[8] Furthermore, it was

Received: August 1, 2024
Revised: September 19, 2024
Accepted: September 25, 2024
Published: October 10, 2024

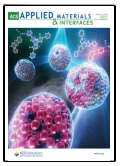

Downloaded via UNIV OF ILLINOIS CHICAGO on June 5, 2025 at 00:11:48 (UTC).
See https://pubs.acs.org/sharingguidelines for options on how to legitimately share published articles.

ACS Publications

© 2024 UChicago Argonne, LLC, Operator of Argonne National Laboratory. Published by American Chemical Society

suggested that "spectator" Mg^{2+} ions could play a pivotal role of keeping the HEO structure intact given that it was inactive in the potential range of interest (>0.01 V vs Li^+/Li).[8,9] Following the same concept, high entropy fluorides (HEF), having similar chemical compositions with the above-mentioned HEO, were synthesized[10] and investigated as a cathode for Li-ion batteries, showing better cycling performance as number of cations increased (higher configurational entropy).[11]

Despite the proposed benefit with a steady structural frame, the presence of electrochemically and electrically inactive spectator ions limit improvement in energy density and could impede charge carrier transport (i.e., electronic conduction), in turn, rate performance.[12] In addition, for conversion reaction where metal cations (e.g., Fe^{2+}) are reduced to metals (e.g., Fe^0) during discharge, unreacted cations result in fewer number of components for configurational entropy, resulting in less favorable structures for entropy stabilization. This work focuses on the role of constituent elements in HEF during conversion reactions, by comparing the newly synthesized high entropy metal fluoride $Co_{0.2}Cu_{0.2}Ni_{0.2}Zn_{0.2}Fe_{0.2}F_2$ (HEF-Fe) and $Co_{0.2}Cu_{0.2}Ni_{0.2}Zn_{0.2}Mg_{0.2}F_2$ (HEF-Mg). The high-entropy metal fluoride (HEF-Fe) replaces the spectator Mg ions with an active Fe ion participant in the conversion reaction. Contrary to the previously proposed benefit from an inactive component, the HEF-Fe showed comparable cycle stability with the HEF-Mg. More importantly, the HEF-Fe provided enhanced discharge capacity and better rate capability due to additional redox ability of Fe (i.e., Fe^{2+} to Fe^{3+}) and potentially better charge transport, which were explored using synchrotron X-ray analysis and density functional theory (DFT) calculations, respectively. Post-mortem high-resolution transmission electron microscopy (TEM) indicated that a steady decrease in capacity with cycles could be associated with segregation of reduced metal (e.g., Cu and Zn). These results emphasize the significance of rational selection of metal cations in HEFs and provide insights for a design guideline to develop multication metal fluorides for high-performing Li-ion battery cathodes.

2. EXPERIMENTAL SECTION

2.1. Materials Preparation and Electrochemical Characterization. The HEF and medium entropy fluoride (MEF) were synthesized by a mechanochemical method using high-energy ball milling. For the targeted HEF and MEF, equimolar weighted metal fluoride powders (CoF_2, CuF_2, NiF_2, ZnF_2, FeF_2, and MgF_2) were mixed in a mortar first, transferred to a stainless-steel jar with stainless-steel balls, and ball-milled for 3 h using SPEX Mill 3000. Then, the synthesized powders were mixed with carbon black (C45, Timcal, 20 wt %)[10] and additionally ball-milled for 3 h to make a metal fluoride−carbon nanocomposite.[4] For comparison, each individual metal fluoride - carbon nanocomposites were prepared under the same condition, and the simple mixture of those was prepared by mildly mixing them in an equimolar ratio in a mortar. Electrodes were prepared by the slurry casting method, with the ink consisting of 85 wt % of active material, 5 wt % carbon black, and 10 wt % polyvinylidene fluoride in *N*-methyl-2-pyrrolidone on Al foil. The electrode films were dried overnight at 110 °C in a vacuum.

Electrochemical coin cell testing was conducted using a 2032 coin cell configuration. The coin cells were composed of a metal fluoride−carbon nanocomposite cathode, GF/F glass fiber separator (Whatman), and Li metal anode (MTI corporation). 1.2 M $LiPF_6$ in EC/EMC (3:7 weight ratio) was used as an electrolyte without an additive. All synthesis and coin cell fabrication procedures were performed in an Ar-filled glovebox to minimize air/moisture exposure. Battery cycling tests were performed using a Maccor battery cycler (Maccor) and electrochemical impedance spectroscopy (EIS) measurements were performed using a Biologic VSP-300 potentiostatic device. For the galvanostatic intermittent titration technique (GITT), the current pulse was applied for 1 h with a current density of 50 mA/g and the cell was relaxed for 3 h. This procedure was repeated between 1.0 and 4.5 V for the initial cycle.

2.2. Materials Characterization. X-ray diffraction (XRD) patterns of metal fluoride carbon nanocomposite powders were measured using a Rigaku Miniflex with a CuKa radiation source (1.5406 Å). X-ray photoelectron spectroscopy (XPS) measurements were measured by using a PHI 5000 VersaProbe II System (Physical Electronics). The spectra were collected using an Al−Kα radiation ($h\nu$ = 1486.6 eV) beam (100 μm, 25 W), Ar^+, and electron beam sample neutralization, in the fixed analyzer transmission mode. Peak fitting was processed using a Shirley background correction and the Gaussian−Lorentzian curve synthesis, available in MultiPack software. XPS spectra were aligned to the carbon black component in the C 1s spectra at 284.8 eV.

Ex situ synchrotron XRD and pair distribution function (PDF) analyses were carried out at the 11-ID-B beamline in the Advanced Photon Source (APS), Argonne National Laboratory (wavelength 0.2115 Å), using a silicon-based area detector. The charged and discharged powder samples were collected from electrode films at the voltage points of interest, rinsed with dimethyl carbonate, and dried in a vacuum in an Ar-filled glovebox. For PDF analysis, the samples were measured in a capillary and data were collected to high values of momentum transfer (20 $Å^{-1}$). PDF, $G(r)$, was extracted from the data using the PDFGetX2,[13] after correcting for background and Compton scattering. X-ray absorption spectroscopy (XAS) measurements, including X-ray absorption near-edge structure (XANES) and extended X-ray absorption fine structure (EXAFS), were performed at the 12BM-B beamline in the APS. Samples were collected from electrode films for ex situ measurements. Operando XAS measurements were carried out in the quick-EXAFS mode using the 2032-coin cell, which had a Kapton-sealed hole at the center for X-ray beam penetration. Co, Cu, Ni, Zn, and Fe K-edge XAS spectra were collected in the transmission mode. The XAS data were processed using Athena software packages.[14]

The microstructures of the metal fluoride nanocomposite powders were characterized by using high-resolution scanning transmission electron microscopy (STEM) and selected-area electron diffraction (SAED). The powders were mixed with acetonitrile and drop-cast on a mesh grid with a lacey carbon support in a glovebox filled with an Ar atmosphere. STEM characterization was conducted using an aberration-corrected JEOL ARM200CF equipped with a cold field-emission electron source, operated at 200 kV. Imaging and spectroscopic measurements were conducted with the emission current at 15 μA, an electron probe semiconvergence angle of 24 mrad, as well as inner and outer detector angles of 68 and 280 mrad for high-angle annular dark imaging.[15] To conduct nanoscale elemental identification and quantification, a JEOL ARM200CF is equipped with an Oxford XMX100TLE X-ray windowless silicon drift detector with a 100 mm^2 detector area for energy-dispersive spectroscopy (EDS).[16] Electron energy-loss spectroscopy (EELS) measurements were conducted using a postcolumns Gatan Continuum GIF ER spectrometer, with an electron probe semiconvergence angle of 17.8 mrad and a collection angle of 53.4 mrad. The elemental compositions of the metal fluoride nanocomposite powders were first investigated with EDS on a large scale and then further distinguished at higher spatial resolutions with EELS. Furthermore, the valence states of the cations included in the metal fluoride powders were analyzed and correlated to the electrochemical process.

2.3. Computation Detail. Atomistic configurations for metal fluoride structures were obtained using the Special Quasirandom Structure (SQS) method,[17] as implemented in the Alloy Theoretic Automated Toolkit.[18] Concisely, a Monte Carlo-based evolutionary algorithm was used to search for a periodic atomic structure whose correlations can closely match the correlation functions of an ideally mixed solid-solution. The HEF rutile phases were modeled as a 120-

https://doi.org/10.1021/acsami.4c12920
ACS Appl. Mater. Interfaces 2024, 16, 57151−57161

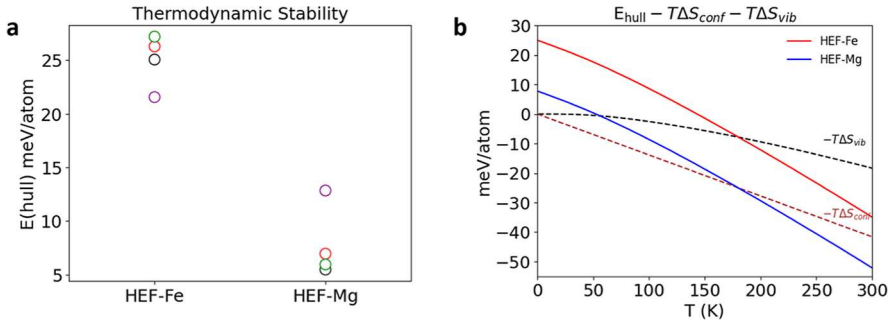

Figure 1. Thermodynamic stability of the studied HEFs. (a) E_{hull} (the energy above the convex hull) for 4 SQS configurations for the HEF-Fe and HEF-Mg. (b) Total Gibbs free energy and entropic contributions (configurational and vibrational) to its values.

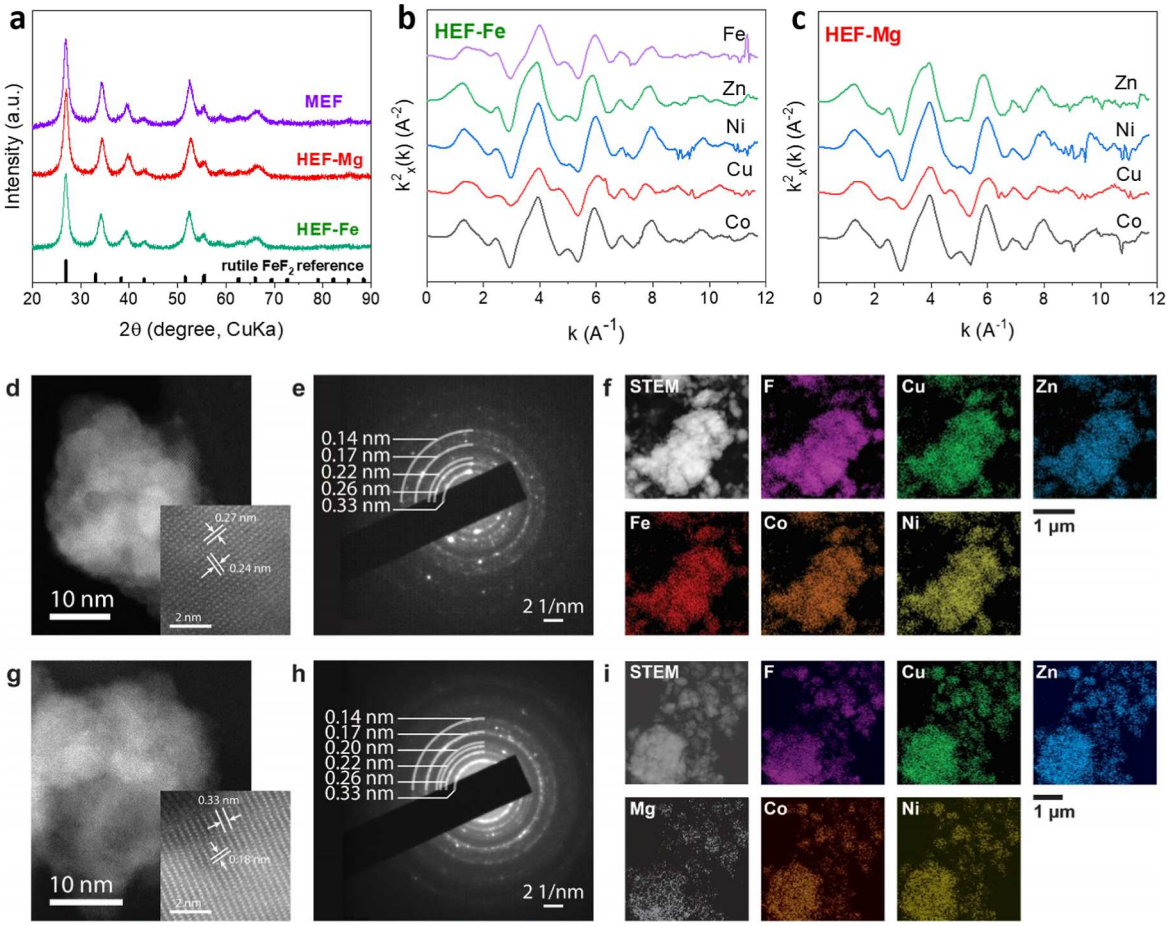

Figure 2. Material characterization of HEF. (a) XRD patterns of the HEF-Fe (green), HEF-Mg (red), and MEF (purple). Rutile FeF_2 reference (ICSD Coll. Code 9166) is provided. EXAFS of the HEF-Fe (b) and HEF-Mg (c), TEM images (d,g), SAED analysis (e,h), and energy-dispersive X-ray spectroscopy (EDS) mapping (f,i) of the HEF-Fe and HEF-Mg, respectively.

atom cell, using 2[100], 2[010], and 5[001] cell vectors, where [100], [010], and [001] represent the conventional rutile basis vectors. The body-centered cubic (BCC) metallic phases were modeled as a 90-atom cell, with 3[100], 3[010], and 5[001] cell vectors, where [100], [010], and [001] represent the conventional BCC basis vectors (see Figure S1 in the Supporting Information).

All DFT calculations were run as implemented in the Vienna Ab initio Simulation Package (VASP)[19] using the projected augmented wave[20] with the generalized gradient approximation of Perdew–Burke–Ernzerhof (PBE).[21] The Hubbard on-site interactions were included for Fe (U = 5.3), Cu (U = 4), Ni (U = 6.2), and Co (U = 3.32) atoms, with values taken from the Materials Project.[22] The kinetic energy cutoff was set to 500 eV. The R_k length of the automatic meshing in VASP was set to 30 Å for both the rutile and BCC SQS structures. The energy convergence criterion of the electronic self-consistency cycle was set to 1×10^{-6} eV for all calculations. Ionic relaxation was terminated when the interatomic forces were less than 1×10^{-2} eV/Å. Vibrational frequency calculations for the alloyed phases and phases on the energy hull were done with stricter tolerance criteria of at least 10^{-8} eV for the total energy and 10^{-8} eV/Å for interatomic forces. The pymatgen[23] library was used to parse the VASP output data.

3. RESULTS AND DISCUSSION

3.1. Thermodynamic Stability of the HEF Materials. The HEF materials were synthesized using primarily mechanical impact energy generated from a high-energy ball

https://doi.org/10.1021/acsami.4c12920
ACS Appl. Mater. Interfaces 2024, 16, 57151−57161

milling process, which has been proven to decrease the particle size as well as to form a composite structure with conducting carbon materials, both of which are necessary for effective battery conversion reaction of metal fluorides.[24] And, a some portion of mechanical energy could be transformed into thermal energy. In order to predict whether synthesized HEF materials would be stable at relevant low temperatures, thermodynamic stability of the HEF materials was investigated on the basis of DFT calculations. First, as shown in Figure 1a, the energy values above the convex hull (E_{hull}) were computed for four representative atomic configurations generated using the SQS method for each composition. For the HEF-Fe with its convex hull made of binary fluorides (CoF_2, CuF_2, NiF_2, ZnF_2, and FeF_2), the E_{hull} at T = 0 K had a spread of ~5.6 meV/atom. On the other hand, the convex hull of the HEF-Mg, constructed from the corresponding binary fluorides (CoF_2, CuF_2, NiF_2, ZnF_2, and MgF_2), resulted in a spread of ~7.3 meV/atom of the E_{hull} at T = 0 K. To calculate HEF stability at a finite temperature, the configurational entropy contribution (S_{conf}), originating from mixing equimolar five cations, was computed with eq 1.

$$S_{conf} = -k_B \sum_{i=1}^{5} p_i \ln(p_i) \tag{1}$$

where k_B is the Boltzmann constant and p_i is the probability of mole fraction of the element in HEF ($\sum_{i=1}^{5} p_i = 1$). The vibrational entropy contribution ($S_{vib,i}$) was also considered because it can either increase or decrease the stability of newly formed phases[25] and calculated using eq 2.

$$S_{vib,i} = \frac{E_i}{k} \frac{\exp\left(-\frac{E_i}{k_B T}\right)}{1 - \exp\left(-\frac{E_i}{k_B T}\right)} - \mathrm{Log}\left(1 - \exp\left(-\frac{E_i}{k_B T}\right)\right) \tag{2}$$

where i runs over all real vibrational frequencies, E_i is the energy of the ith vibrational mode, and T is the temperature. Finally, the total Gibbs free energy for HEF formation was calculated using eq 3.

$$G = E_{hull} - TS_{conf} - TS_{vib} \tag{3}$$

Figure 1b shows the total Gibbs free energies and the entropic corrections to the E_{hull}, computed and averaged over the SQS configurations for the HEF-Fe and HEF-Mg as a function of the temperature. At 300 K, the thermodynamic stability of the HEF-Fe was improved by 41.6 meV/atom due to its configurational entropy contribution to the free energy. The vibrational entropy contributions increased nonlinearly with the temperature, with a contribution of 18.3 meV/atom at 300 K. Total entropic contributions (configurational + vibrational) were as pronounced as 59.9 meV/atom at 300 K in the case of the HEF-Fe, resulting in the increased stability of HEF materials and −34.9 meV/atom of the Gibbs free energy of formation at 300 K. After applying the same values of entropic corrections to HEF-Mg free energy calculations, its Gibbs free energy of formation is reduced to −52.2 meV/atom at 300 K. Figure 1b also shows that the mixing temperature, when the free energy becomes zero, can be as low as 143 and 52.3 K for the HEF-Fe and HEF-Mg, respectively, indicating their synthesizability.

3.2. Synthesis and Characterization of the HEF Materials. As predicted by the DFT calculations, both HEF-Fe and HEF-Mg were successfully synthesized by a mechanochemical method using high-energy ball milling. For comparison, a MEF, $Co_{0.25}Cu_{0.25}Ni_{0.25}Zn_{0.25}F_2$, was also synthesized without containing Fe or Mg. As shown in Figure 2a, XRD confirmed the single-phase rutile structure (the tetragonal $P4_2/mnm$ space group) of as-synthesized HEF-Fe, HEF-Mg, and MEF without noticeable impurities or phase separation. The XRD peaks were broadened due to the decreased grain size by mechanical milling and a disordered crystal structure with the effect of high mixing entropy (see Figure S2 in the Supporting Information for the change in XRD peaks as a function of milling time). The lattice parameters of rutile-structured HEF-Fe and HEF-Mg were found to be $a = b = 4.698$ Å, $c = 3.172$ Å and $a = b = 4.676$ Å, $c = 3.127$ Å, respectively (see Figure S3 in the Supporting Information for Pawley fitting results), while their average crystallite size was estimated to be 239 and 160 nm, respectively. Increased lattice parameters for the HEF-Fe was consistent with a larger ionic radius of Fe^{2+} (78 pm) than Mg^{2+} (72 pm).[25]

The XAS analysis was used to investigate atomic local structure and chemical state of the HEF materials. Figure 2b,c presents the EXAFS in the k-space of the as-synthesized HEF-Fe and HEF-Mg, collected for Co, Cu, Ni, and Zn K-edges, respectively, including the Fe K-edge for the former (see Figure S4 in the Supporting Information for comparison with individual metal fluorides). The short-range environments for all elements were identical, and their local structures were similar to each other, indicating a random cation distribution on average. Moreover, the XANES spectra of all metal components for the HEF-Fe and HEF-Mg were located at the same energy for the corresponding metal(II) fluoride references with a similar peak shape and position (see Figure S5 in the Supporting Information for the XANES K-edge spectra). This indicated that the oxidation state of all cation elements in the as-synthesized HEF-Fe and HEF-Mg were maintained as 2+ during high-energy ball milling without resulting in segregated phases, such as metal particles or further oxidation.

STEM analysis was performed to examine the crystallographic and morphological properties of the as-synthesized HEF-Fe and HEF-Mg powders. STEM characterizations revealed that the HEFs were polycrystalline nanoparticles with particle sizes that ranged between 10 and 100 nm but can form clusters up to hundreds of nanometers. The high-resolution STEM (Figure 2d,g) images showed representative clusters of the nanoparticles and lattice planes from HEF-Fe and HEF-Mg, respectively. In Figure 2d, d-spacings of 0.27 and 0.24 nm were labeled, corresponding to (101) and (111) planes in HEF-Fe. In Figure 2g, d-spacings of 0.33 and 0.18 nm were identified, corresponding to (110) and (211) planes in HEF-Mg, respectively. SAED from representative larger areas is shown in Figure 2e and h. The diffraction rings were labeled with the corresponding lattice spacings and confirmed a rutile structure without any crystalline impurities, which was in accordance with the XRD results. Energy-dispersive X-ray spectroscopy (EDS, Figure 2f,i) analysis of these particles showed that all metallic cations and fluorine were homogeneously distributed in general. However, EELS measurements, providing a higher resolution than EDS, revealed that local cation segregation could exist (Figure S6 in the Supporting Information). For example, some of as-synthesized HEF-Mg particles had local aggregation of Mg, while Co depletion was

https://doi.org/10.1021/acsami.4c12920
ACS Appl. Mater. Interfaces 2024, 16, 57151−57161

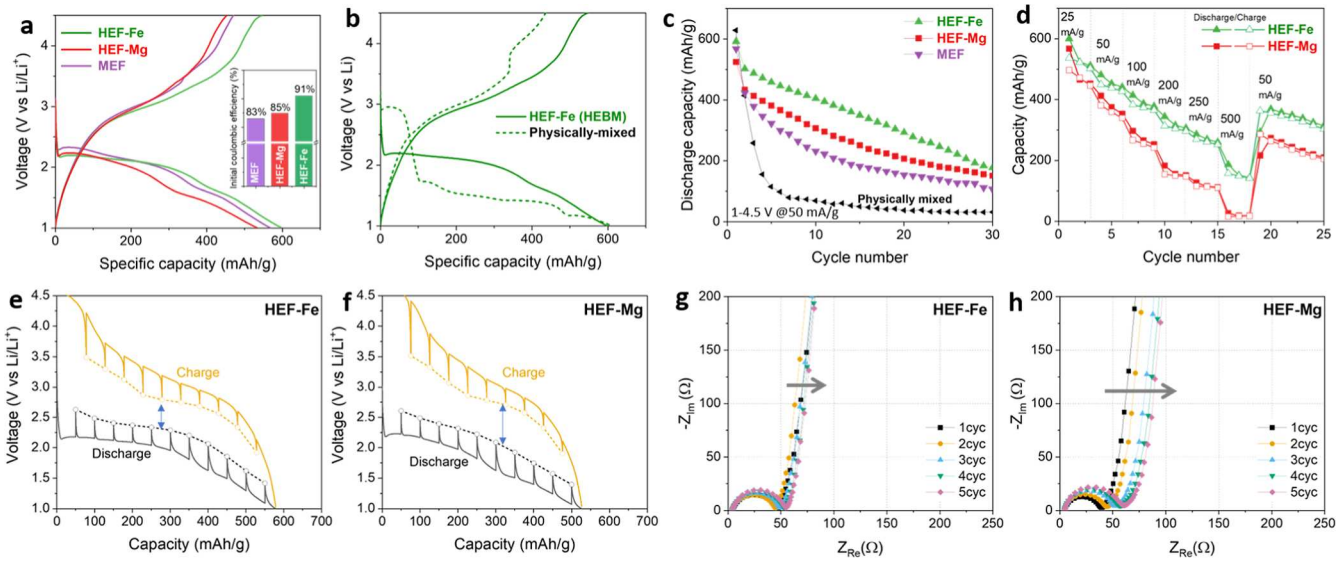

Figure 3. (a) Discharge−charge voltage profiles, (b) comparison with the physically mixed phase, and (c) cycling performance of the HEF-Fe (green), HEF-Mg (red), MEF (purple), and the physically mixed phase (black) electrodes a at current density of 50 mA/g in the voltage range of 1−4.5 V vs Li/Li^+. (d) Rate capability of the HEF-Fe and HEF-Mg electrodes. GITT profile and EIS analysis during the initial 5 cycles of the HEF-Fe (e,g) and HEF-Mg (f,h), respectively.

found in the case of some HEF-Fe particles. Mechanical impact energy and local heating generated during the high-energy ball milling process may not be sufficient to induce complete mixing through high entropy stabilization.

3.3. Electrochemical Performance of the HEF Electrodes. Electrochemical measurements were performed on the HEF materials to evaluate their electrochemical properties in the presence of multiple redox active elements. Figure 3a shows galvanostatic discharge−charge voltage profiles of the HEF-Fe, HEF-Mg, and MEF electrodes for the initial cycle in a half-cell configuration with a Li−metal counter electrode. Upon discharging, these electrodes showed a smooth voltage plateau up to 200−300 mA h g^{-1} below ∼2.3 V, which was followed by decreasing voltage. Differential capacity analysis (dQ/dV) indicated that these broad plateaus were composed of closely located, at least two, redox peaks for the HEFs, while clear separation of peaks were observed for the MEF (see Figure S7 in the Supporting Information). For initial discharge−charge voltage profiles of constituent single metal fluorides (see Figure S8a,b in the Supporting Information), voltage plateau values for the HEFs were lower than the conversion reaction potential of Cu but higher than those of others (Co, Fe, Ni, and Zn). On the other hand, their simple physical mixture showed multistep voltage plateaus corresponding to conversion reaction potentials of each single metal fluoride (Figure 3b). For example, in the mixture, Cu conversion occurred at the beginning of charging around ∼3.0 V. This observation indicated that cooperative redox reaction of atomically mixed multiple cations, located in the same lattice environment, had a significant impact on electrochemical properties of the HEF and MEF materials. In fact, this was different from the case of two components, $(Cu,Fe)F_2$, that a voltage plateau at 2.7−2.9 V, attributed to Cu conversion, was clearly observed when $[Cu] \geq 0.5$.[5] Note that a small fluctuation at ∼1.5 V was believed to originate from electrolyte decomposition related to solid electrolyte interphase (SEI) formation.[3,26]

Conversion voltage of the HEF-Fe and HEF-Mg was estimated on the basis of DFT calculation to corroborate the experimental findings with the following conversion reactions

$$5(Co_{0.2}Cu_{0.2}Ni_{0.2}Zn_{0.2}Fe_{0.2})F_2 + 10Li \leftrightarrows (CoCuNiZnFe)_{BCC} + 10LiF \quad (4\text{-}1)$$

$$5(Co_{0.2}Cu_{0.2}Ni_{0.2}Zn_{0.2}Mg_{0.2})F_2 + 8Li \leftrightarrows (CoCuNiZn)_{BCC} + MgF_2 + 8LiF \quad (4\text{-}2)$$

Here, it is assumed that Mg is not electrochemically active in the voltage regime of this study (1.0−4.5 V). Multication metal fluorides and defluorinated metallic phases were constructed as rutile and BCC phases, respectively. And, the reference states for Li and LiF were assumed to be metallic BCC and cubic ($Fm\bar{3}m$) polymorphs, respectively. The conversion voltages per electron for the HEF-Fe and HEF-Mg were calculated to be 2.502 ± 0.004 and 2.651 ± 0.005 V, averaged over four values corresponding to four SQS rutile structures, respectively. These estimated values for conversion voltages were reasonably consistent with the experimentally obtained ones, given that overpotentials were commonly observed due to kinetically limited conversion reactions.[4]

During the charging process for the HEF-Fe, HEF-Mg, and MEF, in addition to the voltage plateau at ∼3 V, a higher voltage plateau at 3.3−3.5 V was observed (Figure 3a and dQ/dV plots for Figure S7 in the Supporting Information). The lower voltage plateau is likely attributed to M^0/M^{2+} oxidation of metallic components, while the higher voltage plateau can be associated with Cu oxidation. Indicating that Cu conversion no longer fully remained in a collective redox reaction with other cations due to considerable agglomeration during the preceding discharge process. For the HEF-Fe, the second plateau at ∼3.4 V can be also attributed to further oxidation of Fe from 2+ to 3+ state,[5,27] which will be discussed more in detail later.

Galvanostatic discharge of the HEF-Fe electrode over 1.0−4.5 V resulted in 599 mA h g^{-1} of an initial discharge capacity,

https://doi.org/10.1021/acsami.4c12920
ACS Appl. Mater. Interfaces 2024, 16, 57151−57161

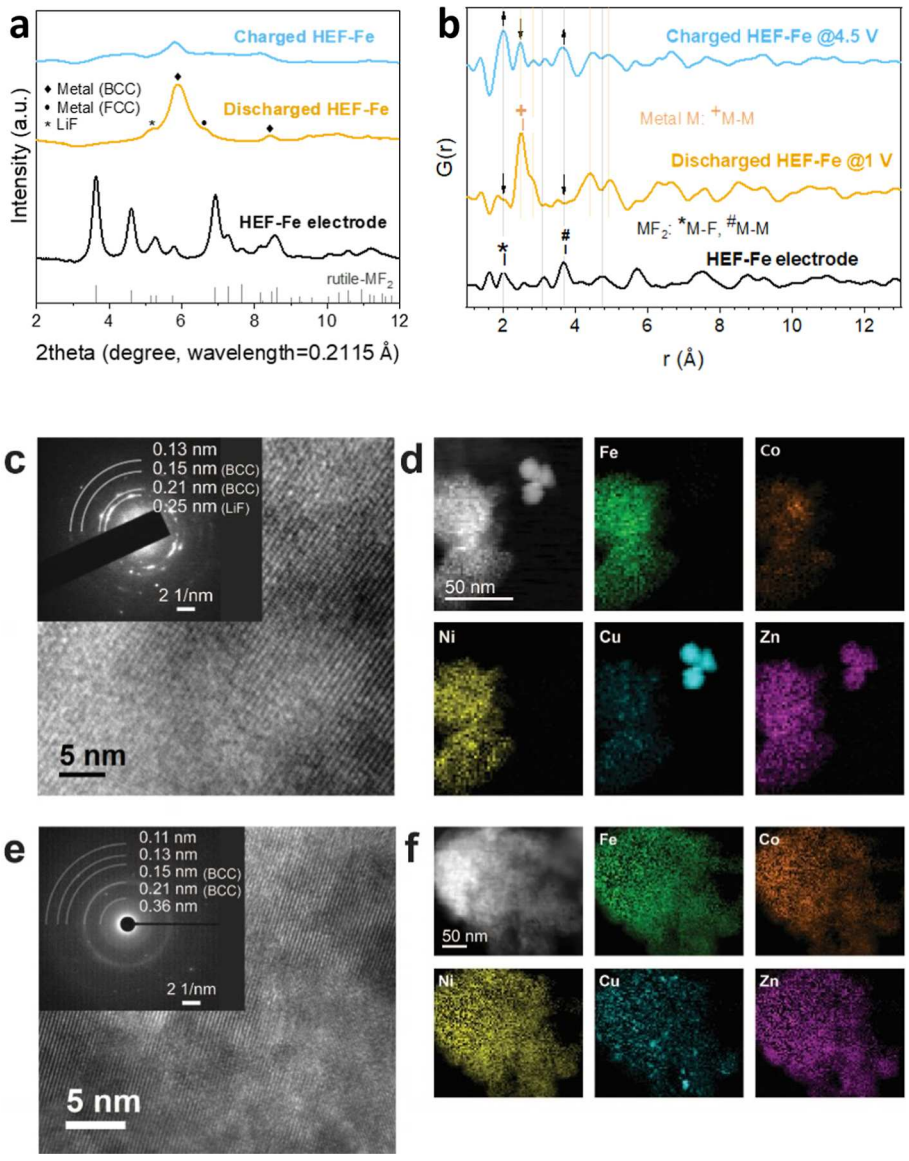

Figure 4. Ex situ XRD (a) and PDF (b) analyses of the discharged and charged HEF-Fe compared to its pristine state. Dotted lines and arrows are provided to guide peak location and intensity change. TEM images and EELS mapping of the HEF-Fe after first discharge (c,d) and charge (e,f), respectively.

comparable to the theoretical value (544 mA h g^{-1}), with ~91% of the initial Coulombic efficiency (ICE). The HEF-Mg electrode showed a lower initial discharge capacity value (534 mA h g^{-1}) due to electrochemically inactive Mg (its theoretical value is 465 mA h g^{-1}) as well as lower ICE (~85%) than the HEF-Fe. Lastly, the MEF electrode showed 568 mA h g^{-1} of initial discharge capacity (its theoretical value is 538 mA h g^{-1}), similar to the HEF-Fe but a much lower ICE (~83%). These results indicated that entropy-driven stabilization for reversible conversion reaction was enhanced by increase in the numbers of cations. This is corroborated with better initial battery cyclability of the HEFs, compared to the MEF electrodes and physical mixture (Figure 3c). After 30 cycles, each fluoride cathode sample delivered a discharge capacity of 177 mA h/g for the HEF-Fe, 151 mA h/g for the HEF-Mg, and 106 mA h/g for the MEF, whereas the physical mixture and most of the single metal fluorides showed poorer capacity retention under the same condition (see Figure S8c in the Supporting Information). Here, interestingly, the HEF-Fe showed a similar cycling performance with HEF-Mg even though the former did not take potential advantage of structural stability due to an electrochemically inactive element as some literature hypothesized.

In addition to higher discharge capacity, HEF-Fe outperformed HEF-Mg in terms of the rate capability performance, as shown in Figure 3d. The HEF-Fe delivered higher capacity as the applied current density increased and after returning to the slow current of 50 mA/g. Another interesting feature in the HEF-Fe's improved electrochemical performance was a smaller voltage hysteresis. The voltage hysteresis of the HEF-Fe and HEF-Mg was measured by using the GITT, as shown in Figure 3e and f, respectively. The average voltage gap between charge and discharge was reduced to 0.63 V for the HEF-Fe, compared to 0.71 V for the HEF-Mg. This could be related to the more facile electronic conduction in HEF-Fe than HEF-Mg. As shown in Figure S9, the instantaneous IR drop and diffusion coefficient were calculated from the GITT results, and the results show that HEF-Fe has a lower

https://doi.org/10.1021/acsami.4c12920
ACS Appl. Mater. Interfaces 2024, 16, 57151−57161

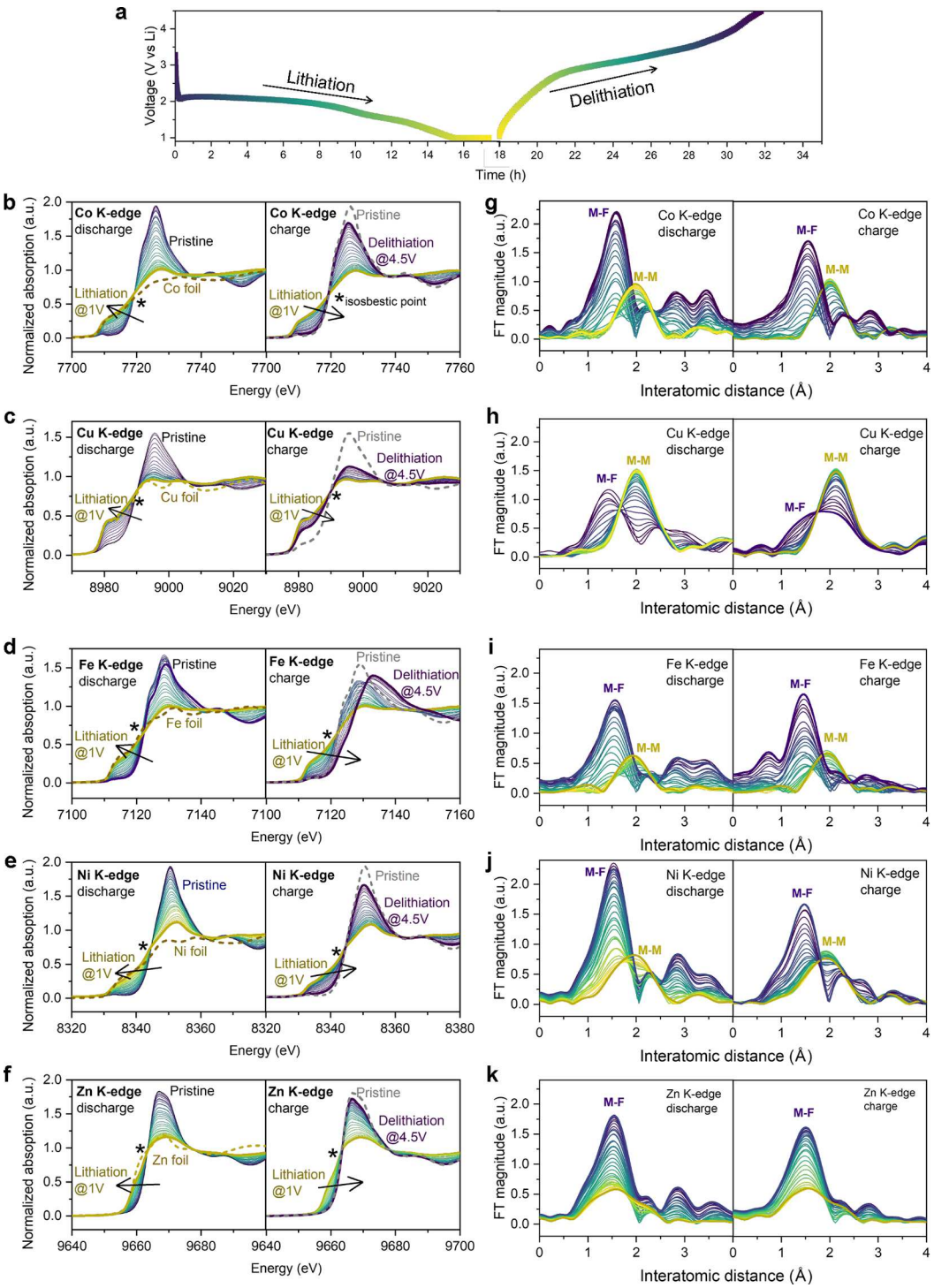

Figure 5. (a) Voltage profile of the HEF-Fe for the first cycle during in situ XAS measurements. (b–f) Co, Cu, Fe, Ni, and Zn K-edge XANES spectra and (g–k) corresponding Fourier transformation (FT) of EXAFS (not phase corrected) during initial discharging and charging processes. The spectra of Co, Cu, Fe, Ni, and Zn metals are also shown for reference.

resistance and better performance. Based on electronic density of state (DOS) evaluated with DFT calculations, HEF-Fe was expected to have a ∼ 2.0 eV of energy band gap with several defect states, while the HEF-Mg was found to have a larger ∼2.82 eV of band gap with defect states centered at ∼1 eV above the Fermi level (see Figure S10 and the text in the Supporting Information). Overall, the DOS data indicated that HEF-Fe was expected to be more electronically conducting than HEF-Mg, suggesting better electrochemical cell performance.

EIS was conducted for the HEF-Fe and HEF-Mg with a Li counter electrode in a half-cell system (Figure 3g,h). Their EIS spectra showed a high-frequency semicircle, which could be assigned with combination of interfacial resistance due to SEI layer formation and charge-transfer resistance, followed by a sloping straight line indicative of capacitive nature at a low-frequency regime. As the cycle number increased, a gradual

https://doi.org/10.1021/acsami.4c12920
ACS Appl. Mater. Interfaces 2024, 16, 57151−57161

resistance increase was observed in the HEF-Mg, which might be attributed to capacity fading. The electrode surface might be degraded due to electrode−electrolyte side reaction and unstable SEI formation (see Figure S11 and the text in the Supporting Information).[28] However, HEF-Fe was more stable compared to HEF-Mg during this initial cycling. All these observations suggested that the electrochemical behavior of multication metal fluorides was influenced not only by entropy-driven structural stabilization with numbers of constituent cations but was also greatly affected by its constituent cations.

3.4. Ex Situ XRD-PDF and TEM Analysis on the HEF-Fe Electrodes. Synchrotron high energy XRD and PDF analyses were performed to better understand the structural change during Li storage into HEF-Fe. Figure 4a presents XRD results of the discharged (orange line) and charged (blue line) HEF-Fe, compared to its pristine state (black line). The initial rutile structure converted to the BCC metallic structure after discharge (lithiated), as observed by the new broad reflections centered at ∼5.9° increasing, corresponding to the growth of the (110) plane of the BCC metallic structure. A diffraction peak (2θ = ∼6.6°) related to the BCC (face-centered cubic) structure was also observed for the discharged electrode, which could be related to the aggregation of Cu metal. After subsequent charge, the reflection of the metallic phase reduced, but the peaks related to the initial rutile structure were not restored at the end of the delithiation process.

As typically observed for conversion materials, a nanoscale reaction product with small domain sizes and highly disordered nature could not be captured in XRD. Therefore, complementary PDF analyses were performed to detect phase transformation at an atomic scale. As shown in Figure 4b, for the as-synthesized HEF-Fe, the peak at 2.02 Å corresponded to the M-F bonds, while the one at 3.68 Å reflected the M−M bond in a rutile metal fluoride structure.[4] For the discharged HEF-Fe, the new peaks at 2.51, 2.85, and 4.41 Å, which could be assigned to the M−M distance in the BCC phase, appeared indicating the formation of metal species. Interestingly, after subsequent charge processes, reappearance of the peak associated with M−F bonds was clearly observed, while the peaks related to the BCC metallic phase showed a decrease in intensity (see Figure S12 in the Supporting Information and rough estimation of the ratio between phases). These observations indicated that a reversible conversion reaction was achieved in a short-range order for the HEF-Fe electrodes. Consistent with XRD results, the features associated with the metallic phase still remained, suggesting metal species were not fully reoxidized during the charge process.

Ex situ TEM measurements were also performed to investigate the atomic scale phase transition of the HEF-Fe electrode during the discharging−charging process. As shown in the SAED in Figure 4c, when discharged to 1.0 V, HEF-Fe exhibited crystallinity, and the SAED images of this sample (from representative clusters of the powders) showed diffraction rings for *d*-spacings of 0.21 and 0.15 nm, corresponding to the planes in the BCC metallic phase; LiF is detected with the diffraction ring at a *d*-spacing of 0.25 nm, indicating the conversion reaction. EELS maps on the discharged HEF-Fe (Figure 4d) showed a homogeneous distribution of metal ions at large. However, it was also found that some metals like Cu and Zn were locally segregated, which could be associated with irreversible capacity loss. When charged back to 4.5 V, the spacing in the SAED rings (Figure 4e) showed both peaks from the pristine HEF-Fe (*d*-spacing of 0.36 nm) and the peaks in the charged XRD, indicating reversible formation of the crystalline rutile phase and remaining metal phase during the delithiation process, respectively. Crystallinity can also be confirmed from direct imaging (Figure 4e). As shown in the EELS maps of the charged HEF-Fe (Figure 4f), most of the metal cations were still well distributed over cathode particles, while Cu remained as nanoscale agglomerates (see Figure S13 and the text in the Supporting Information for the EELS spectra). These observations were consistent with ones from the above-mentioned X-ray scattering measurements.

3.5. In Situ XAS on the HEF Electrodes. In situ elemental specific XAS measurements were performed on both HEF electrodes in order to monitor change in the valence state and local structural reorganization of metal cations and thus to gain insights into redox behaviors of multication metal fluoride. Figure 5 summarizes the HEF-Fe's XANES and EXAFS results of transition metals (Co, Cu, Ni, Zn, and Fe) K-edges along with the voltage profile during the first discharge−charge cycle (see the results for the HEF-Mg electrode in Figure S14 in the Supporting Information).

During discharge (lithiation) from the open circuit voltage to 1 V, the XANES spectra of five cations in the HEF-Fe (left panels of Figure 5b−f) clearly show a continuous shift in the absorption edge to lower energy (metal foil reference region). This indicates that the average valence states of all cations decreased from 2+ to metallic state (0), confirming the formation of the metallic phase after lithiation, which was in agreement with the other characterization results. Appearance of metallic states were also observed by an intensity increase of low energy edge shoulder at approximately 7712, 8982, 8335, 9659, and 7115 eV for Co, Cu, Ni, Zn, and Fe K-edge, respectively, as discharge proceeded. Isosbestic points appeared in all spectra suggesting a two-phase transition between dissociation of M-F bonds and formation of M−M bonds. This was corroborated by the FT of the EXAFS analysis (left panels of Figure 5g−k). The peak intensity related to the M−F bond decreased while the one for the M−M bond increased during lithiation. For the HEF-Mg, electrochemically active four cations (Co, Cu, Ni, and Zn) showed similar redox behavior with the ones in the HEF-Fe.

A closer look at these XAS measurement results revealed element-specific redox behavior in the single-step voltage plateau (see Figure S15 in the Supporting Information for the charge-dependent change in oxidation states of each cation determined from a half-height energy position). On discharge, for both HEF-Fe and HEF-Mg, reduction of Cu was completed earlier, while that of the other four cations continued until the voltage reached 1 V. Interestingly, conversion reactions of the other cations (Co, Ni, Fe, and Zn) were activated at higher voltages (∼2 V), compared to the ones in their individual metal fluoride (see Figure S8a). This suggested that a multication-mixed environment could create a cooperative redox reaction between constituent elements, boosting reaction kinetics. In fact, in $Cu_{0.5}Fe_{0.5}F_2$, it was also observed that Cu-oxidation occurred together with Fe-oxidation at much lower potential (∼1.5 V) than an expected value (>3 V).[5]

On charge back to 4.5 V, the in situ XAS results revealed element-specific redox behavior during the reconversion (delithiation) process. As for Co, Ni, and Zn (the right panels

https://doi.org/10.1021/acsami.4c12920
ACS Appl. Mater. Interfaces 2024, 16, 57151−57161

of Figure 5b,e,f for the HEF-Fe and Figure S13b,d,e for the HEF-Mg), absorption edges in the XANES spectra show a continuous shift toward higher energy, indicating oxidation of metals back to their original states (M^{2+}). This reversible conversion reaction was corroborated with the corresponding FT EXAFS data (the right panels of Figure 5g,j,k for the HEF-Fe and Figure S14f,h,I for the HEF-Mg), which displayed the disappearance of the M−M bond peak with reformation of the M−F bond peak.

On the other hand, the XANES spectra of Cu (the right panel of Figure 5c for the HEF-Fe and Figure S14c for the HEF-Mg) started to show an edge shift toward higher energy only at a high voltage region (>3.5 V) and did not come back to its pristine metal fluoride state, indicating that its reconversion reaction was not fully reversible. This incomplete oxidation of Cu was supported by its FT EXAFS data (the right panel of Figure 5h for the HEF-Fe and Figure S14g for the HEF-Mg), which showed an overlap between the M−F bond peak and the remaining M−M bond peak. As observed in the ex situ TEM results (Figure 4f), this unreacted metallic Cu seemed to be segregated, forming nanoscale particles in the HEF matrix. Interestingly, partially oxidized Cu was found to be reversibly reduced during the subsequent lithiation (see Figure S16), which was in contrast to pure CuF_2.[3] The existing M−F rutile-like framework evolved in multication metal fluorides at a lower voltage may facilitate nucleation of Cu−F bond.[5] In addition to entropy stabilization, this reversible Cu redox behavior may contribute to better battery cycling performance of the HEFs, compared with pure CuF_2 (see Figure S8c).

Lastly, the additional electrochemically active ion, Fe, in the HEF-Fe presented quite different redox behavior compared to other elements. The change in the Fe K-edge XANES spectra (the right panel of Figure 5d) indicated that the Fe-oxidation state gradually increased from 0 to 2+ during the initial stage of charge. Then, further oxidation of Fe^{2+} to Fe^{3+} was observed at higher potential, as the absorption edge shifted to higher energies than the one for its pristine state. This was in agreement with the dQ/dV plot, which presented the redox peak at ∼3.4 V during charge. It was found that Fe^{3+} was reversibly reduced back to Fe^0 during subsequent lithiation at the second cycle (see Figure S16). This extra redox capability of Fe in HEF-Fe compensated for capacity loss due to partial Cu redox activity, resulting in higher discharge capacity and Coulombic efficiency compared to those of the HEF-Mg.

4. CONCLUSIONS

In this work, the high entropy fluoride, $Co_{0.2}Cu_{0.2}Ni_{0.2}Zn_{0.2}Fe_{0.2}F_2$ (HEF-Fe), was newly synthesized by a simple mechanochemical route and compared with $Co_{0.2}Cu_{0.2}Ni_{0.2}Zn_{0.2}Mg_{0.2}F_2$ (HEF-Mg) to study the role of constituent elements in a high-entropy material; specifically, functionality of electrochemically inactive and active cation for the battery conversion reaction. While HEF-Mg is a widely studied transition-metal composition with Mg as a spectator; HEF-Fe was designed to contain five active participants for the conversion reaction. Both HEFs showed a better battery performance, in terms of discharge capacity and cyclability, than the metal fluoride with four cations and the simple mixture, confirming that entropy stabilization could facilitate a reversible conversion reaction with lithium. Reversible evolution in crystallinity and structure of the HEF particles during conversion reaction were verified by high-resolution microscopy. Interestingly, contrary to the proposed advantage with an inactive component to stabilize the initial lattice framework, replacing Mg with Fe resulted in an insignificant impact on battery cycle stability. On the other hand, HEF-Fe delivered a higher discharge capacity with a higher ICE than HEF-Mg. In operando XAS revealed that this improvement was related to a reversible wide redox range of Fe with overoxidation to Fe^{3+}, as compensating the irreversibility of Cu redox reaction. In addition, this elemental specific technique uncovered that a multication-mixed environment in HEF could create cooperative redox reaction between constituent elements and thus boost reaction kinetics. Moreover, HEF-Fe showed a lower voltage hysteresis and enhanced rate capability, which could be related to its improved electronic charge transport, as the DFT calculated electronic structures suggested. Lastly, change in impedance with cycles indicated that the electrode−electrolyte interface of the HEF-Fe was more stable. These results highlighted that rational cation selection for multielement metal fluorides can pave the way to improve their battery performance. Long-term cyclability still remains a challenge, but this rich flexibility in design space, together with intrinsically high capacity and potential use of earth-abundant elements, can make entropy-stabilized conversion-type metal fluorides appealing electrode candidates for next-generation lithium-ion batteries.

■ ASSOCIATED CONTENT

Supporting Information

The Supporting Information is available free of charge at https://pubs.acs.org/doi/10.1021/acsami.4c12920.

DFT calculation, XRD, PDF, XAS, and high-resolution transmission electron microscopy experimental results collected for HEF-Fe and HEF-Mg materials, XPS spectra of electrode from the cycled HEF-Fe and HEF-Mg cells, and electrochemical results (PDF)

■ AUTHOR INFORMATION

Corresponding Authors

Jehee Park − *Chemical Sciences and Engineering Division, Argonne National Laboratory, Lemont, Illinois 60439, United States;* Present Address: Department of Chemical and Biological Engineering, Hanbat National University, Yuseong-Gu, Daejeon, 34158, Republic of Korea; orcid.org/0009-0000-7817-5351; Email: jeheep@hanbat.ac.kr

Jae Jin Kim − *Chemical Sciences and Engineering Division, Argonne National Laboratory, Lemont, Illinois 60439, United States;* orcid.org/0000-0001-7709-3530; Email: jaekim@anl.gov

Authors

Yingjie Yang − *Department of Physics, University of Illinois -Chicago, Chicago, Illinois 60607, United States;* orcid.org/0000-0002-1898-8171

Haesun Park − *School of Integrative Engineering, Chung-Ang University, Seoul 06974, Republic of Korea;* orcid.org/0000-0001-6266-8151

Aditya Sundar − *Materials Science Division, Argonne National Laboratory, Lemont, Illinois 60439, United States*

Sungsik Lee − *X-ray Science Division, Argonne National Laboratory, Lemont, Illinois 60439, United States;* orcid.org/0000-0002-1425-9852

https://doi.org/10.1021/acsami.4c12920
ACS Appl. Mater. Interfaces 2024, 16, 57151−57161

Tiffany L. Kinnibrugh − *X-ray Science Division, Argonne National Laboratory, Lemont, Illinois 60439, United States*
Seoung-bum Son − *Chemical Sciences and Engineering Division, Argonne National Laboratory, Lemont, Illinois 60439, United States;* orcid.org/0000-0002-3723-6186
Eungje Lee − *Chemical Sciences and Engineering Division, Argonne National Laboratory, Lemont, Illinois 60439, United States;* orcid.org/0000-0003-3647-1595
Peter Zapol − *Materials Science Division, Argonne National Laboratory, Lemont, Illinois 60439, United States;* orcid.org/0000-0003-0570-9169
Robert F. Klie − *Department of Physics, University of Illinois -Chicago, Chicago, Illinois 60607, United States;* orcid.org/0000-0003-4773-6667

Complete contact information is available at: https://pubs.acs.org/10.1021/acsami.4c12920

Author Contributions

The manuscript was written through contributions of all authors. All authors have given approval to the final version of the manuscript.

Notes

The authors declare no competing financial interest.

■ ACKNOWLEDGMENTS

This material is based upon work supported by Laboratory Directed Research and Development (LDRD) funding from Argonne National Laboratory, provided by the Director, Office of Science, of the U.S. Department of Energy under contract no. DE-AC02-06CH11357. Use of the Advanced Photon Source (the beamline 11-ID-B and 12-BM-B), a U.S. Department of Energy (DOE) Office of Science user facility at Argonne National Laboratory, was supported by the U.S. DOE Office of Science, Office of Science, Office of Basic Energy Sciences, under contract no. DE-AC02-06CH11357. The authors acknowledge the computing resources provided on Bebop, a high-performance computing cluster operated by the Laboratory Computing Resource Center at Argonne National Laboratory. RFK was supported by a grant from National Science Foundation (DMR-2309396). YY and RFK made use of instruments in the Electron Microscopy Service, specifically JEOL JEM-ARM200CF in the Research Resources Center, University of Illinois at Chicago. The acquisition of UIC JEOL JEM-ARM200CF was supported by an MRI-R2 grant from the National Science Foundation (DMR-0959470) and the upgraded Gatan Continuum spectrometer was supported by a grant from the NSF (DMR-1626065).

■ REFERENCES

(1) (a) Olbrich, L. F.; Xiao, A. W.; Pasta, M. Conversion-type fluoride cathodes: current state of the art. *Curr. Opin. Electrochem.* **2021**, *30*, 100779. (b) Wang, L.; Wu, Z.; Zou, J.; Gao, P.; Niu, X.; Li, H.; Chen, L. Li-free Cathode Materials for High Energy Density Lithium Batteries. *Joule* **2019**, *3* (9), 2086−2102.
(2) (a) Sun, L.; Li, Y.; Feng, W. Metal Fluoride Cathode Materials for Lithium Rechargeable Batteries: Focus on Iron Fluorides. *Small Methods* **2023**, *7* (2), 2201152. (b) Hua, X.; Eggeman, A. S.; Castillo-Martínez, E.; Robert, R.; Geddes, H. S.; Lu, Z.; Pickard, C. J.; Meng, W.; Wiaderek, K. M.; Pereira, N.; et al. Revisiting metal fluorides as lithium-ion battery cathodes. *Nat. Mater.* **2021**, *20* (6), 841−850.
(3) Hua, X.; Robert, R.; Du, L.-S.; Wiaderek, K. M.; Leskes, M.; Chapman, K. W.; Chupas, P. J.; Grey, C. P. Comprehensive Study of the CuF2 Conversion Reaction Mechanism in a Lithium Ion Battery. *J. Phys. Chem. C* **2014**, *118* (28), 15169−15184.
(4) Wang, F.; Robert, R.; Chernova, N. A.; Pereira, N.; Omenya, F.; Badway, F.; Hua, X.; Ruotolo, M.; Zhang, R.; Wu, L.; et al. Conversion Reaction Mechanisms in Lithium Ion Batteries: Study of the Binary Metal Fluoride Electrodes. *J. Am. Chem. Soc.* **2011**, *133* (46), 18828−18836.
(5) Wang, F.; Kim, S.-W.; Seo, D.-H.; Kang, K.; Wang, L.; Su, D.; Vajo, J. J.; Wang, J.; Graetz, J. Ternary metal fluorides as high-energy cathodes with low cycling hysteresis. *Nat. Commun.* **2015**, *6* (1), 6668.
(6) Ma, Y.; Ma, Y.; Wang, Q.; Schweidler, S.; Botros, M.; Fu, T.; Hahn, H.; Brezesinski, T.; Breitung, B. High-entropy energy materials: challenges and new opportunities. *Energy Environ. Sci.* **2021**, *14* (5), 2883−2905.
(7) Rost, C. M.; Sachet, E.; Borman, T.; Moballegh, A.; Dickey, E. C.; Hou, D.; Jones, J. L.; Curtarolo, S.; Maria, J.-P. Entropy-stabilized oxides. *Nat. Commun.* **2015**, *6* (1), 8485.
(8) Sarkar, A.; Velasco, L.; Wang, D.; Wang, Q.; Talasila, G.; de Biasi, L.; Kübel, C.; Brezesinski, T.; Bhattacharya, S. S.; Hahn, H.; et al. High entropy oxides for reversible energy storage. *Nat. Commun.* **2018**, *9* (1), 3400.
(9) Qiu, N.; Chen, H.; Yang, Z.; Sun, S.; Wang, Y.; Cui, Y. A high entropy oxide (Mg0.2Co0.2Ni0.2Cu0.2Zn0.2O) with superior lithium storage performance. *J. Alloys Compd.* **2019**, *777*, 767−774.
(10) Sukkurji, P. A.; Cui, Y.; Lee, S.; Wang, K.; Azmi, R.; Sarkar, A.; Indris, S.; Bhattacharya, S. S.; Kruk, R.; Hahn, H.; et al. Mechanochemical synthesis of novel rutile-type high entropy fluorides for electrocatalysis. *J. Mater. Chem. A* **2021**, *9* (14), 8998−9009.
(11) Cui, Y.; Sukkurji, P. A.; Wang, K.; Azmi, R.; Nunn, A. M.; Hahn, H.; Breitung, B.; Ting, Y.-Y.; Kowalski, P. M.; Kaghazchi, P.; et al. High entropy fluorides as conversion cathodes with tailorable electrochemical performance. *J. Energy Chem.* **2022**, *72*, 342−351.
(12) (a) Gong, C.; Bai, Y.-J.; Qi, Y.-X.; Lun, N.; Feng, J. Preparation of carbon-coated MgFe2O4 with excellent cycling and rate performance. *Electrochim. Acta* **2013**, *90*, 119−127. (b) Reddy, M. V.; Subba Rao, G. V.; Chowdari, B. V. R. Metal Oxides and Oxysalts as Anode Materials for Li Ion Batteries. *Chem. Rev.* **2013**, *113* (7), 5364−5457.
(13) Qiu, X.; Thompson, J. W.; Billinge, S. J. PDFgetX2: a GUI-driven program to obtain the pair distribution function from X-ray powder diffraction data. *J. Appl. Crystallogr.* **2004**, *37* (4), 678.
(14) Ravel, B.; Newville, M. ATHENA, ARTEMIS, HEPHAESTUS: data analysis for X-ray absorption spectroscopy using IFEFFIT. *J. Synchrotron Radiat.* **2005**, *12* (4), 537−541.
(15) Klie, R. F.; Gulec, A.; Guo, Z.; Paulauskas, T.; Qiao, Q.; Tao, R.; Wang, C.; Low, K. B.; Nicholls, A. W.; Phillips, P. J. The new JEOL JEM-ARM200CF at the University of Illinois at Chicago. *Cryst. Res. Technol.* **2014**, *49* (9), 653−662.
(16) Phillips, P. J.; Paulauskas, T.; Rowlands, N.; Nicholls, A. W.; Low, K.-B.; Bhadare, S.; Klie, R. F. A New Silicon Drift Detector for High Spatial Resolution STEM-XEDS: Performance and Applications. *Microsc. Microanal.* **2014**, *20* (4), 1046−1052.
(17) Zunger, A.; Wei, S.-H.; Ferreira, L.; Bernard, J. E. Special quasirandom structures. *Phys. Rev. Lett.* **1990**, *65* (3), 353−356.
(18) Van de Walle, A.; Tiwary, P.; De Jong, M.; Olmsted, D.; Asta, M.; Dick, A.; Shin, D.; Wang, Y.; Chen, L.-Q.; Liu, Z.-K. Efficient stochastic generation of special quasirandom structures. *Calphad* **2013**, *42*, 13−18.
(19) (a) Kresse, G.; Hafner, J. Ab initio molecular dynamics for liquid metals. *Phys. Rev. B* **1993**, *47* (1), 558−561. (b) Kresse, G.; Joubert, D. From ultrasoft pseudopotentials to the projector augmented-wave method. *Phys. Rev. B: Condens. Matter Mater. Phys.* **1999**, *59* (3), 1758−1775.
(20) Blöchl, P. E. Projector augmented-wave method. *Phys. Rev. B* **1994**, *50* (24), 17953−17979.
(21) Perdew, J. P.; Burke, K.; Ernzerhof, M. Generalized gradient approximation made simple. *Phys. Rev. Lett.* **1996**, *77* (18), 3865−3868.

(22) Jain, A.; Ong, S. P.; Hautier, G.; Chen, W.; Richards, W. D.; Dacek, S.; Cholia, S.; Gunter, D.; Skinner, D.; Ceder, G.; et al. Commentary: The Materials Project: A materials genome approach to accelerating materials innovation. *APL Mater.* **2013**, *1* (1), 011002.
(23) Ong, S. P.; Richards, W. D.; Jain, A.; Hautier, G.; Kocher, M.; Cholia, S.; Gunter, D.; Chevrier, V. L.; Persson, K. A.; Ceder, G. Python Materials Genomics (pymatgen): A robust, open-source python library for materials analysis. *Comput. Mater. Sci.* **2013**, *68*, 314−319.
(24) Badway, F.; Pereira, N.; Cosandey, F.; Amatucci, G. G. Carbon-Metal Fluoride Nanocomposites. *J. Electrochem. Soc.* **2003**, *150* (9), A1209.
(25) Shannon, R. D. Revised effective ionic radii and systematic studies of interatomic distances in halides and chalcogenides. *Acta Crystallogr., Sect. A: Cryst. Phys., Diffr., Theor. Gen. Crystallogr.* **1976**, *32* (5), 751−767.
(26) Huang, Q.; Pollard, T. P.; Ren, X.; Kim, D.; Magasinski, A.; Borodin, O.; Yushin, G. Fading Mechanisms and Voltage Hysteresis in FeF2−NiF2 Solid Solution Cathodes for Lithium and Lithium-Ion Batteries. *Small* **2019**, *15* (6), 1804670.
(27) Yamakawa, N.; Jiang, M.; Key, B.; Grey, C. P. Identifying the Local Structures Formed during Lithiation of the Conversion Material, Iron Fluoride, in a Li Ion Battery: A Solid-State NMR, X-ray Diffraction, and Pair Distribution Function Analysis Study. *J. Am. Chem. Soc.* **2009**, *131* (30), 10525−10536.
(28) Senoh, H.; Matsui, K.; Shikano, M.; Okumura, T.; Kiuchi, H.; Shimoda, K.; Yamanaka, K.; Ohta, T.; Fukunaga, T.; Sakaebe, H.; et al. Degradation Mechanism of Conversion-Type Iron Trifluoride: Toward Improvement of Cycle Performance. *ACS Appl. Mater. Interfaces* **2019**, *11* (34), 30959−30967.

https://doi.org/10.1021/acsami.4c12920
ACS Appl. Mater. Interfaces 2024, 16, 57151−57161